Proceedings of Global Power and Propulsion Society
ISSN-Nr: 2504-4400
GPPS Chania24
September 4-6, 2024
www.gpps.global

GPPS-TC-2024-041

INVESTIGATION OF THE INFLUENCE OF DIFFERENT ROTOR COMPONENTS ON THE AXIAL IMPELLER TIP CLEARANCE AT DIFFERENT OPERATING POINTS

Martino Köhler
German Aerospace Center (DLR)
Institute of Low Carbon Industrial Processes
martino.koehler@dlr.de
Zittau, Saxony, Germany

Robert Schaffrath
German Aerospace Center (DLR)
Institute of Low Carbon Industrial Processes
robert.schaffrath@dlr.de
Zittau, Saxony, Germany

Michael Lockan
German Aerospace Center (DLR)
Institute of Low Carbon Industrial Processes
michael.lockan@dlr.de
Cottbus, Brandenburg, Germany

Eberhard Nicke
German Aerospace Center (DLR)
Institute of Low Carbon Industrial Processes
eberhard.nicke@dlr.de
Zittau, Saxony, Germany

ABSTRACT

This work examines a radial turbo-compressor for a high-temperature heat pump (HTHP) with steam as the working medium. The given boundary conditions result in very small blade heights for the impellers. It is therefore necessary to minimize the gap between the impeller and housing in order to ensure the lowest possible gap flow. It is to be expected that even small deviations towards a larger gap have a major negative impact on the performance of the compressor. Nevertheless, a collision must also be avoided. In order to find efficient and reliable impeller designs an automated optimization is performed considering aerodynamic as well structural aspects (Schaffrath et al., 2022). However, the optimal impeller design represents the so-called hot geometry under operating conditions, for the manufacturing process this geometry have to be transformed into the so-called cold geometry (Schaffrath et al., 2023). Due to the necessary quality of detail in the gap maintenance, the question arises as to whether it is sufficient to execute the hot-to-cold transformation exclusively on the impeller and whether there is a significant influence of the other components of the rotating system. The FE simulation is used to compare the maximum axial deformation values between the design of the single impeller and the entire rotating system. The result shows a deviation in axial deformation of more than 50% compared to the result of the ”hot-to-cold transformation” (H2C) used in optimization process chain. This shows that the single impeller calculation is not sufficient to precisely achieve the gap on which the CFD design is based.

INTRODUCTION

There is an overwhelming consensus on the need to reduce CO_2 emissions to achieve politically agreed climate goals. The generation of process heat for industry, more than 90% of which is still generated by combustion of fossil fuels, accounts for a large share of CO_2 emissions. In order to maintain the economic performance of an industrialized nation and at the same time reduce the combustion of fossil fuels, the utilization of waste heat from a variety of industrial processes is necessary. High Temperature Heat Pumps (HTHPs) are promising technology for providing process heat, required e.g. in the paper and food industry or other insustries using drying processes. The first systems are already reaching a temperature level of 300°C. Temperatures of up to 500°C are considered realistically achievable for the next generations of HTHPs (Schwarzburger and Alfons.W.GentnerVerlag, 2022).In Germany alone, there is a CO_2 savings potential of around 38 million tons in the temperature range between 100°C and 500°C (Umweltbundesamt, 2024) and (Maaß et al., 2018), which is equivalent to the total CO_2 emissions of Switzerland (myclimate foundation and Dellantonio, 2022). Due to the compact design and the relatively high efficiency, HTHPs can be equipped with radial turbo compressors (Casey and Robinson, 2021). In order to exploit the advantages of the turbo radial compressor system, it is necessary to individually optimize each compressor

design with regard to fluid mechanical, structural mechanical and rotodynamic requirements, which is an interdisciplinary task. The Institute of Low Carbon Industrial Processes uses especially developed optimization processes for this purpose, which is described in (Schaffrath et al., 2022) and (Schaffrath et al., 2023). The result of this process is an optimized design at a defined operating point, i.e. under the effect of all loads in the same point. The aero performance calculated in the optimization process can only be achieved in real operation if the assumed geometric boundary conditions occur during operation. Assuming that one of the most important factors influencing the aerodynamic performance of the compressor, characterized by pressure ratio and isentropic efficiency, is the gap between the impeller and housing, which is called "tip clearance". Many studies in the past have shown the influence of tip clearance on the aero-performance characteristics and it is a well-known fact that increasing the tip clearance has a negative influence on this performance due to gap flows or a changed downstream flow angle (Danish et al., 2006). In the field of micro gas turbines, the influence of mechanical and thermal loads has been investigated (Wang and Xi, 2009). However, these findings are usually not fully considered when designing the cold impeller geometry using hot to cold (H2C) analysis (Hazby et al., 2015). In contrast to previous work, the focus of the current study is on the components surrounding the impeller and their arrangement. The aim is to show what influence the integration of the impeller into the rotating assembly has on tip clearance during operation. Another special feature is the impeller geometry generated from the optimization, which is characterised by low blade heights and thus a short hub length as well as a contoured rear side of the supporting disc. In general, the cold geometry represents the component to be manufactured.
The theory behind the H2C-process is described in the section Theoretical background of the H2C analysis. For further use, it is necessary to convert the finite-elemente-mesh of the cold geometry into a surface or solid model. The procedure of reverse engineering is described in section Generation of "cold geometry" from mesh data file. In order to answer the question of whether it is sufficient to include only the impeller geometry in the tip clearance analysis or what influence the design conditions have on it, the paper is divided into the following structure. In the first section, the methodical procedure is explained using the specific example. A comparison of the solvers used is made, a reasonable mesh quality is determined and the generation of the cold geometry is explained in sections Influence of the mesh and mesh study and Influence from the solver. In the next section, the modeling of the FE model is discussed in detail, followed by the validation and evaluation of the H2C results from the CSM process chain. The focus here is on the influences of the selected methodological approach and the external influences of the design conditions. This is followed by the calculation of the deformations considering the complete rotating system of the compressor and the resulting tip clearance values at several operating points. The results are evaluated in the final part of the investigations with regard to the influencing load components and their influence on the aerodynamic performance of the compressor.

METHODOLOGY

In order to create a simulation model that considers the conditions of the assembly design of the rotating part of the compressor and thus provides more accurate results compared to the calculation of the individual part, various steps must be carried out. A particular focus here is on the influences of geometry, FE meshes and FE solvers used. Furthermore, deviating load assumptions resulting from the assembly generation must be included in the modeling. The steps described in detail in the following sections are summarized graphically in Figure 1.

Initial situation

The starting point for the investigations of the rotating system with regard to its deformation and thus the influence on tip clearance is the blade geometry of the hot impeller geometry, that means the geometry under full load condition, as well as the mesh data file of the cold impeller geometry of the blade and disk. In these investigations, cold geometry always refers to the unloaded geometry. The surface of the hot geometry is already available as a STEP-file, generated by DLR's internal BladeGen software. All data originate from the automated optimization process, which is described in detail in (Schaffrath et al., 2022) and (Schaffrath et al., 2023). Further input data for the overall model, such as the impeller hub geometry of the impeller, the geometry of neighboring components, the type of bearing or information on material data are part of the compressor design process, here selected from the design of an existing compressor, which is discussed in more detail in FE-modelling: Model with fully designed impeller geometry.

Theoretical background of the H2C analysis

H2C analyses are usually carried out exclusively on the impeller geometry (Hazby et al., 2015). A common method for H2C analyses is to build an initial FE-mesh FE_H based on the hot geometry and to apply the corresponding load to the mesh-nodes PC_H. In many cases, only the rotational velocity is used as the load (Hazby et al., 2015), whereas in this study the pressure and temperature distribution are also considered as additional load components. The nodal displacements δ_0 of the individual mesh-nodes PC_H are then subtracted from the coordinates of the hot mesh FE_h to generate an initial cold mesh FE_c^0. The FE calculation is performed again with FE_c^0 and the node displacement δ^i with $i = (1....n)$ is determined. A new hot mesh FE_H^i with the point coordinates PC_H^i is created. If the convergence criterion

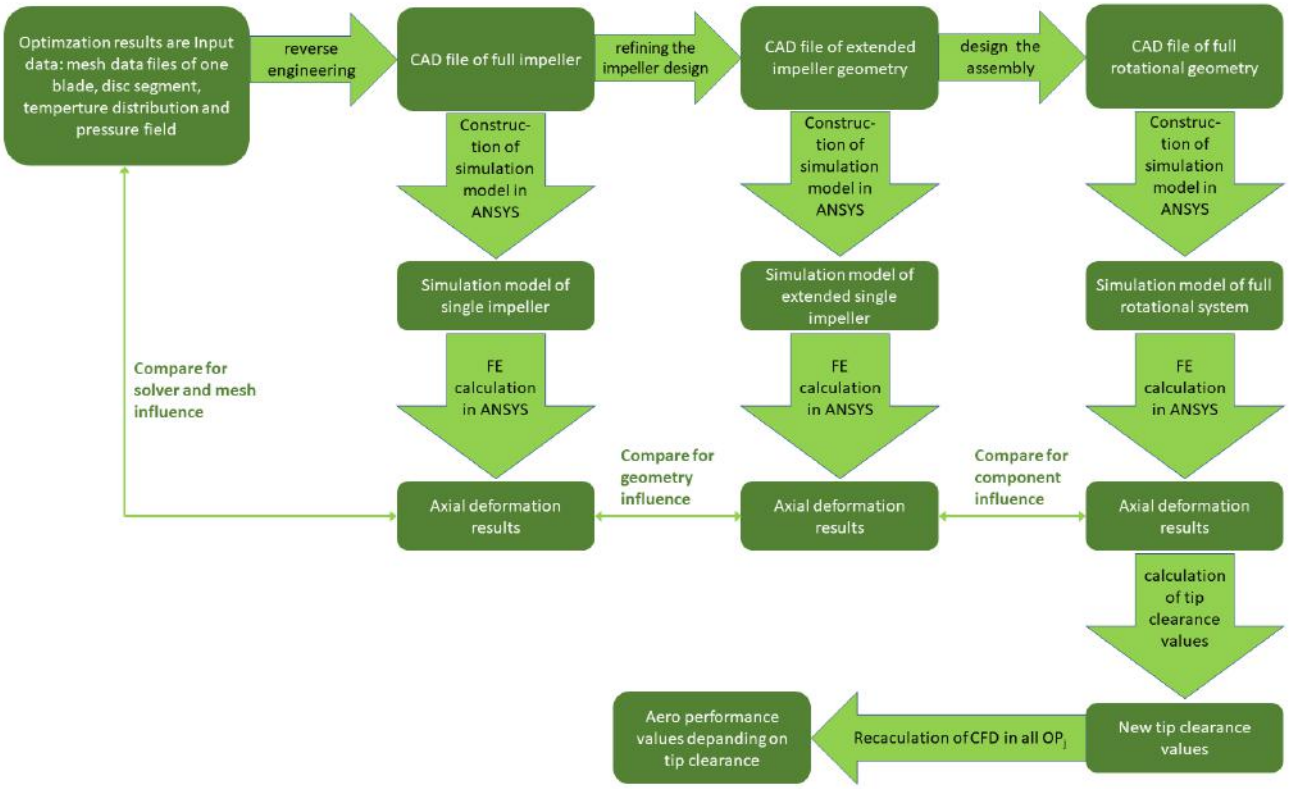

Figure 1 Schematic representation of the steps required to evaluate the aerodynamic performance at various operating points under the influence of the impeller design conditions

$$PC_H - PC_H^i < 0,1mm \tag{1}$$

is reached, the calculation is aborted and FE_c^0 corresponds to the final cold geometry. If it is not reached, a further iteration is carried out with FE_c^i as the initial mesh.(Hazby et al., 2015). The convergence criterion of 0.1 mm was selected for the present study in order to reduce the number of iterations required and must be regarded as rough. In the case of manufacturing the component, it is recommended that the criterion be reduced by a factor of 10. The value would then be a tenth of the usual minimum manufacturing tolerance of ± 0.05 mm

Generation of a CAD file of cold geometry from mesh data files

To use the cold geometry, it is necessary to convert the various sub-meshes from the CSM part of the optimization process chain into a geometry description consisting of surfaces described by B-splines. The process described in the next paragraph, developed by (Gaun et al., 2014), is used for this purpose. The implementation is carried out using CATIA V5 software.

If the model of the hot geometry consists of surfaces described by B-splines or NURBs, the FE mesh of the cold geometry can be regarded as a displacement field. By shifting the B-spline control points of the description of the hot geometry using the displacement field, the surfaces of the cold geometry can be generated. The method works by breaking down the hot geometry into partial surfaces and identifying the mesh nodes. The FE displacement field is then applied to the projected mesh nodes. Finally, the displacements of the control points are determined by solving linear fitting problems. To achieve the required positional and tangential continuity, a special treatment of the boundary curves and their neighbouring control points is applied (Gaun et al., 2014). The procedure is known as the morphing method and is available in various CAD systems. In the case of this optimization geometry, the CATIA V5 system is used.

The mesh of one blade of the impeller and the mesh of the disk segment are treated separately and merged at the end. All data is located in the same coordinate system, which defines the x-axis as the axis of rotation.

In the first sub-process, the surface of the hot blade geometry and the point cloud, representing the mesh nodes, of the cold blade geometry are imported. By analyzing the deviation of the mesh nodes from the surface, a vector field is generated, which forms the basis for shifting the b-spline control points. A tolerance of 0.003 mm was selected for the current geometry, but a smoothing factor of 0.3 was also set to control the length of the polygon lines between the control points. The result is a surface that represents the cold geometry mesh with the corresponding tolerance. The aim of the surface quality must

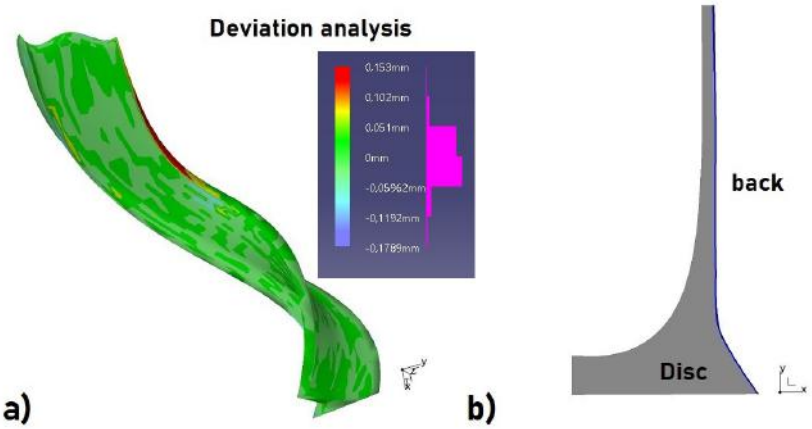

Figure 2 deviation of the morphed blade surface of the cold geometry from the input mesh data (a) and generated rotational spline (blue) of the disc back of the cold geometry (b)

be to keep the deviation of the surface control points from the mesh nodes as small as possible and to generate a normal distribution of the deviation around zero. Emphasis was placed on minimizing the deviation in the area of the largest expected deformation. Figure 2 (a) shows that this could be achieved, although the deviation of the surface from the mesh nodes increases in the direction of the hub.

In the second sub-process of geometry generation, the shell area of the disc is generated from a projected point cloud of the disc segment. Various steps in CATIA V5 are used to generate a surface from the imported point cloud, the boundary curve of which is created. The part of the curve representing the back of the disc, shown as blue spline in Figure 2(b), can now be rotated and therefore forms the basis of the surface of the support disc.

In the third and final sub-process of geometry generation, the solid body of the impeller is created as a full model in CAD, shown in Figure 3. To do this, the line profile of the supporting disc is rotated 360° around the x-axis and the shell area is closed. The morphed surface of the blade is then also closed, patterned into 19 blades at 360° and attached to the support disc using Boolean operations. This fundamentally finalizes the geometry of the impeller. Further constructive additions, which are caused by the integration of the impeller into the assembly design, will be made at a later stage, described in Abstraction of the relevant geometry from the assembly.

Influence of the mesh and mesh study on deformation results

In the CSM process chain, a composite mesh is used that is generated in two different meshing tools, which proves to be disadvantageous in the connection area of the meshes using contacts by Multi Point Constraint procedure (MPC). In contrast, a coherent mesh is used to calculate the assembly. The mesher integrated in ANSYS is used for this purpose (ANSYS, 2023). The mesh was made from the elements SOLID187, a 3-D 10-node homogeneous structural solid element (és Gazdaságtudományi Egyetem, 2018). The reference is no longer explicitly stated when elements used are subsequently

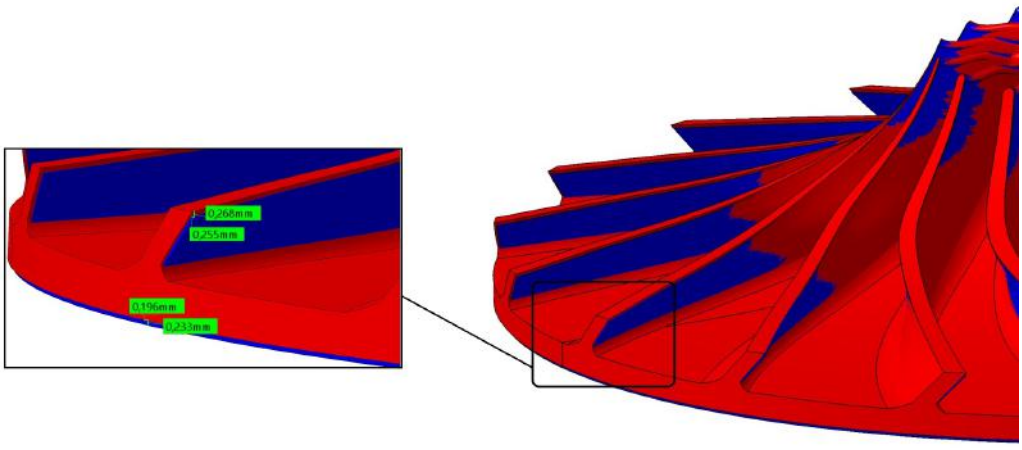

Figure 3 CAD result of hot (red) and cold (blue) Impeller-Geometry

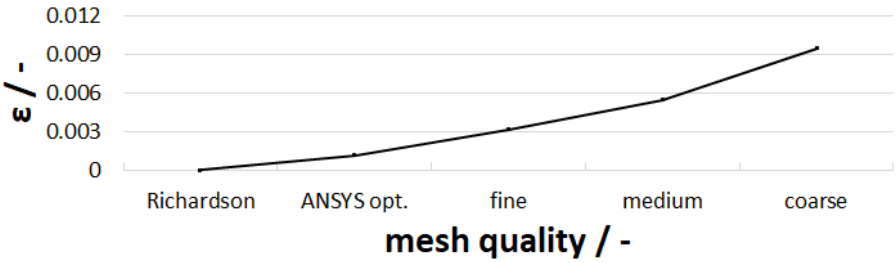

Figure 4 RELATIVE ERRORS BETWEEN DIFFERENT MESH RESOLUTIONS AND RICHARDSON EXTRAPOLATION

mentioned. The quality of this new mesh has to be evaluated. Once, the model is recalculated with this mesh under the same conditions as in the CSM process chain and the results are compared. At the same time, a mesh study is carried out using the Richardson method (Slater, 2021). The theory behind this can be described by:

$$E = c \cdot h^B \tag{2}$$

where E represents the error, B the convergence order and h the spatial discretization.
The Richardson approach starts with a mesh of any quality, estimated by personal experience, which is refined in two stages with a refinement ratio r of approximately 1.2. An FE simulation is carried out with each of these meshes. The maximum value of axial deformation $\delta_x max$ is used as the evaluation parameter, which is generally denoted by f in Equation 3, using the Richardson extrapolation method. The result of which is based on an infinitesimally fine mesh, forms the comparison criterion for evaluating the mesh quality. The derivation of the Richardson extrapolation and grid convergence as an evaluation method is derived and explained in the literature (Schaffrath et al., 2023), (Roache, 1994) and (Slater, 2021). The results can be seen in Table 1.

$$f_{h=0} = f_{fine} + \frac{f_{fine} - f_{medium}}{r^p - 1} \tag{3}$$

$$p = \frac{\ln\left(\frac{f_{coarse} - f_{medium}}{f_{medium} - f_{fine}}\right)}{\ln(r)} \tag{4}$$

One more FE-mesh, called ANSYS opt, is evaluated in Table 1. It results from the use of automated mesh refinement, controlled by the result accuracy. For this, a convergence is assigned to the result of the maximum axial deformation δ_{xmax} to be evaluated. The value is usually between one and five percent. Here, the convergence limit is defined as three percent. This means that the mesh is refined until the change in the controlling result value falls below the convergence limit. This requires the use of the iterative solver. The result is closest to the theoretical result of the Richardson extrapolation and therefore shows the smallest relative error. The relative errors of the individual meshes compared to the infinitesimally fine mesh are shown in Figure 4. The relative error of the mesh optimized by ANSYS compared to the infinitesimal small mesh is below 0.2% and therefore acceptable. The computing time is quadrupled, but the computing times are still economically unproblematic. This mesh is therefore used for further calculations.

Influence from the solver on deformation results

The FE calculations within the CSM process chain are carried out using the ”CALCULIX” (Dhondt, 2022) solver and a two-part mesh consisting of two different meshers. The sub-meshes of disc and blade are connected using MPC contacts (Schaffrath et al., 2023). This setup is not suitable for calculating an assembly. Therefore, the assembly is calculated with ”ANSYS Mechanical”, using ANSYS’ own mesher. In order to know the error caused by the different solvers and meshes of the two models, a geometrically identical model is calculated in ANSYS Mechanical with regard to the boundary conditions.

Table 1 RESULTS OF GRID CONVERGENCE STUDY FOR IMPELLER GEOMETRY

	RICARDSON	COARSE	MEDIUM	FINE	ANSYS OPT
$n_{elements}$		73,634	98,346	129,406	461,943
n_{nodes}		136,701	179,959	236,056	714,730
δx_{max} / mm	0.25490	0.25248	0.25350	0.25409	0.25460
t_{calc} / s		23	27	34	149
rel. error ε of δx_{max}	0	0.00949	0.00549	0.00316	0.00118

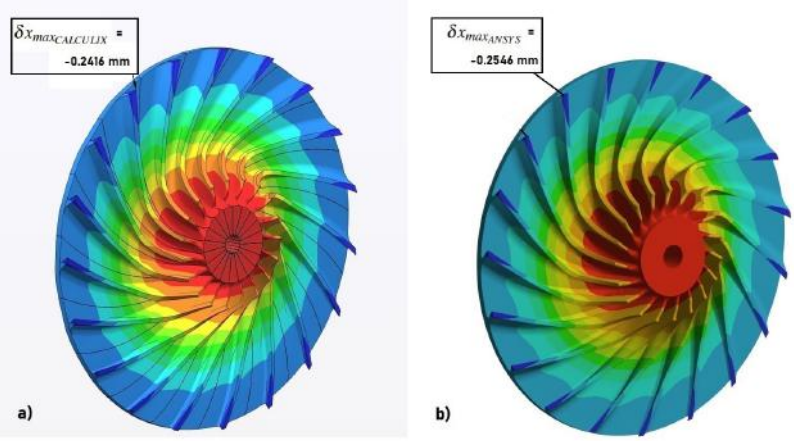

Figure 5 maximum axial deformation CLACULIX (a) and maximum axial deformation ANSYS (b)

Figure 5 shows the respective results of the two solvers. A high degree of agreement can be seen. With regard to the distribution of values across the geometry, no significant difference can be seen. The maximum value of the axial deformation $|\delta x_{max}|$ is calculated to 0.2416 mm in CALCULIX and 0.2541 mm in ANSYS, which results in an absolute deviation $|\Delta\delta x_{max_{Solver}}|$ of 0.013 mm. This value is calculated as the difference between the two values of the maximum axial deformations of the respective solver, defined by:

$$\Delta\delta x_{max_{Solver}} = |\delta x_{max_{ANSYS}}| - |\delta x_{max_{CALCULIX}}| \tag{5}$$

The relative error between the two models $\varepsilon_{rel_{Solver}}$, defined as the quotient of the absolute deviation of the maximum axial deformation and the absolute value of the maximal axial deformation in ANSYS-Solver, calculated by:

$$\varepsilon_{rel_{Solver}} = \frac{|\Delta\delta x_{max_{Solver}}|}{|\delta x_{max_{ANSYS}}|} \tag{6}$$

It is therefore 5.1%. The distribution of the shares of the error from mesh change and solver change is not examined. In relation to the deviation caused by the design conditions of the impeller, the error can be assessed as acceptable. For future calculations, the influence of the error due to the CSM process chain mesh should be significantly reduced by eliminating the sub-meshes and using a continuous mesh.

FE-Model with fully designed impeller geometry

The first step in analyzing the complete rotating system is to build a model with a fully designed impeller. The main change to the calculations in the CSM process chain is that all geometries required for mounting the impeller in its final assembly are integrated in this model. An example of this is the hub geometry for mounting the impeller on the shaft. Furthermore, the gas load in the rear impeller chamber $p_{2s_{red}}$ is added in this model, shown in Figure 6. According to (Zhihua et al., 2022), it is set at 80% of the back-pressure at compressor outlet p_{2s} as described with:

$$p_{2s_{red}} = 0.8 \cdot p_{2s} \tag{7}$$

The boundary conditions still correspond to those described in section FE modelling.

Abstraction of the relevant geometry from the assembly for FE model

To create the model, it is necessary to reduce the geometry to the essentials. The starting point is the CAD data set of the entire compressor assembly. Only the components of the rotating system, consisting of impeller, shaft, bearings, rotor, support ring and clamping set, are considered for the FE model. The individual components are reduced to the necessary geometric details. In this way, small radii, chamfers and other contours are eliminated. Figure 7 shows the full geometric model to be meshed.

FE modelling

All the basic steps for the CSM were developed and described in the previous sections. In the following, the FE model for the entire rotating system of the compressor stage is developed. The materials used in the calculation model correspond to the real design in consultation with the supplier. Table 5 shows the data in detail. The allocation of the materials to the individual components is shown in Figure 7.

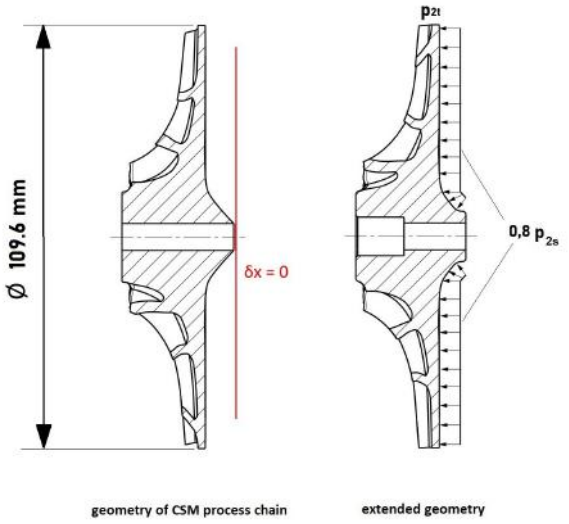

Figure 6 Representation of the geometric and modelling extensions

The mesh for the impeller results from the previous mesh study and is applied directly. In addition, all other components of the rotating system have to be meshed. The mesh should have a sufficiently high quality and still be kept as small as possible in terms of the number of elements. The simple rotationally symmetrical components bearing Inner shell of ball bearing, Shaft, Support ring and Clamping rings are therefore meshed with higher order hexahedra with 20 nodes, using SOLID 186 elements. All other components are meshed with SOLID187 elements, a higher order tetrahedral element with 10 nodes. The complete mesh comprises 674,332 elements with 1,395,645 nodes, without contact elements.
To calculate the assembly, it is necessary to abstract the connection types of the components from reality into the FE model. The knowledge of the real conditions comes from the production drawings and statements from the compressor supplier. In the FE model, the meshed components are connected by means of contact elements. Element types conta174 and targe170 are used for all non-rigid contacts. The “bonded-contact” is mapped using the MPC method. An overview of the contacts used is shown in Table 6.
Positioning in 3D space takes place via the bearing points. The ball bearings are modeled by defining the stiffness and damping matrix. Due to a lack of valid values for damping, only the stiffness matrix is defined in the model. The values are provided by the supplier of the bearings. For the static-mechanical calculation, the rotation around the axis of rotation is blocked at the end of the shaft.
In contrast to the individual part design of the impeller, different states have to be distinguished when calculating deformations of the assembly model. Even when stationary, loads act on the system. By mounting the impeller using a clamping

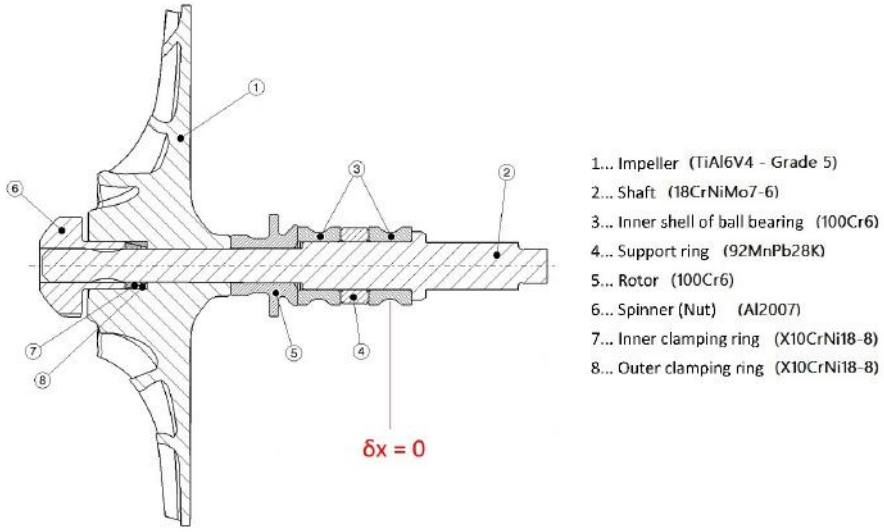

Figure 7 rotating system of the radial compressor stage

Table 2 load values for FE-model at different operation points

	UNIT	OP03	OP02	OP01
bolt pretension F_M	N	4370	4370	4370
rotational speed n_{rot}	rpm	70,000	85,000	105,000
constant low temperature ϑ_l	°C	150	150	150
constant high temperature ϑ_h	°C	198	223	257
temperature at compressor inlet ϑ_{1t}	°C	144	142	142
temperature at compressor outlet ϑ_{2t}	°C	198	223	257
total pressure at compressor inlet p_{1t}	bar(a)	2.93	2.44	2.19
total pressure at compressor outlet p_{2t}	bar(a)	5.06	5.67	6.72
pressure in rear impeller chamber $p_{2s_{red}}$	bar(a)	4.00	4.54	5.40

system, the assembly is under preload. The tightening torque of 8.6 Nm is applied by means of a preload force, which is calculated by (Decker et al., 2011):

$$F_M = \frac{0.16 \cdot P + 0.58 \cdot \mu_G \cdot D_2 + \mu_k \cdot R_m}{M_A} \tag{8}$$

The numerator of the equation contains the geometric dimensions of the screw used, the pitch P, the pitch diameter D_2 of the thread and the friction in the thread μ_G. In addition, the geometry of the screw head is included in the numerator through the mean bearing radius R_m, as well as the friction in this by μ_K. The denominator is the tightening torque M_A of the screw. This state forms load step one in the FE model. Based on this, the loads are now applied that arise from the operation of the compressor. These are the rotational speed of 105,000 rpm in the design point, the pressure field on the blades, a constant pressure $p_{2s_{red}}$ in the rear impeller chamber, calculated by Equation 7, and the temperature distribution in the gas mapped over the entire geometry of the impeller. Due to the absence of heat transfer coefficients and the resulting lack of thermomechanical coupling calculation, the temperature field of the gas is applied to the geometry and kept constant over the cross-section of the impeller. The pressure and temperature fields originate from the CFD simulation within the optimization process chain. The data generated for the impeller segment is rotated by 360° and mapped to the new mesh of the full impeller model. All other components of the rotating system are subjected to a constant temperature. Two cases, which represent the upper and lower limits, are calculated one after the other. The lower limit ϑ_l is slightly above the temperature at the compressor inlet, while the upper limit ϑ_h is defined by the temperature at the impeller outlet. The load is applied in the form of ramps over several load steps. The exact numerical values of the loads at the investigated operating points, also in the partial load range, are listed in Table 2, sorted by ascending rotational speed.

RESULTS AND DISCUSSION

In this section, the results of all simulation calculations are presented and analysed with regard to their effect on tip clearance. The axial deformation results from the calculations of the extended single-impeller model serve as a new basis for comparison in order to evaluate the pure influences of the components of the rotating system. All deviations from the results of the optimisation process chain are therefore no longer included in the comparison.
The effect of individual loads on the tip clearance is shown depending on the operating point and gives an impression of the importance of taking the respective load into account when designing the tip clearance. Finally, the influence of the new tip clearances on the performance of the compressor is shown.

Results of the calculation of fully designed single impeller

In the design phase leading up to the finished component, the geometry must be adapted to the design conditions compared to the design process chain and take into account restrictions from other disciplines. This includes, for example, the connection to the drive shaft. The comparison of both geometries is shown in Figure 6. Furthermore, the gas load in the rear impeller chamber $p_{2s_{red}}$ is added to the model according to Equation 7. In this specific case, it can be seen that the influence of the geometric interference is very small compared to the influence of the additionally considered pressure load. The values are shown in Table 3. It results in an increase in axial deformation of 44% in total.

Table 3 Influence of the extended modelling on the axial deformation

	UNIT	Design geometry optimisation (old reference)	customized geometry	additional load $p_{2s_{red}}$ (new reference)
max. axial deformation δx_{max}	mm	0.2546	0.2618	0.3659
deviation to reference model $\Delta\delta x_{max_{MODEL}}$	mm	0.00	0.0077	0.1118
rel. deviation to reference model $\varepsilon_{rel_{MODEL}}$	%	0.00	3.03	44.00

Results of the rotating system

The first finding from the calculations of the overall system, compared with the results of the single impeller simulation, is the different zero-point position due to the positioning of the axial bearings in the assembly. While the bearing point is defined at the rear hub end face in the single impeller calculation, precisely this face shifts axially in the assembly as a result of the loads, which consequently has an influence on the characteristics of the tip clearance. Section (a) in Figure 8 visualizes the zero offset. The maximum axial deformation of the impeller is located at the impeller outlet. A second general effect is a small rotational asymmetry in the displacements. The reason for this is the mounting of the impeller on the shaft using clamping rings, which are not closed at one point on the circumference and cannot transmit any torques in this area. It is visualized in Figure 8(b).

When considering the complete rotating system, an increase in tip clearance can be seen at all operating points compared to the single impeller calculation. The resulting maximum gap values, which are assumed to be constant and forms the tip clearance, are calculated from the sum of the tip clearance assumed in the CFD s_{CFD} and the deformation of the cold impeller from the H2C analysis s_{H2C} minus the maximum axial deformation of the impeller in the assembly δx_{max}:

$$s_{calc} = s_{CFD} + s_{H2C} - \delta x_{max} \tag{9}$$

and shown in Table 4. The described zero-point shift plays a decisive role in the evaluation of the results. The shares of the loads in the formation of tip clearance s_{calc} are analyzed in more detail in Shares of the individual loads in the axial deformation.

If you now look at the relative deviation of the calculated tip clearance of the rotating system (M_2) from the single impeller model (M_1), we see a significant increase in the same, depending on the assumed shaft temperature. The higher the shaft temperature is assumed (M_3), the smaller the tip clearance becomes, but it is still greater than if only the impeller is considered. At this point, the distance of the impeller from the bearing point, and thus the thermal shaft expansion, has a major influence on the final result of the tip clearance. In relation to the operating points analyzed, the relative deviation of the tip clearance from the reference model increases with increasing speed. The percentage deviation of the calculated tip

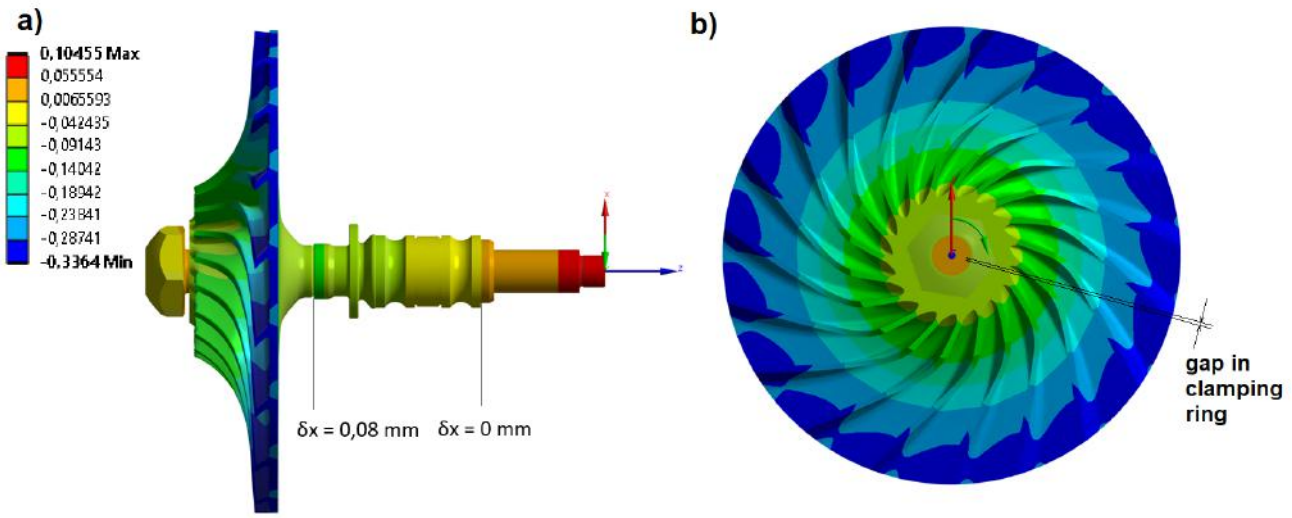

Figure 8 Zero offset when calculating the complete rotating assembly (a) and asymmetry due to gap in the circumference of the spring washer in the clamping system (b)

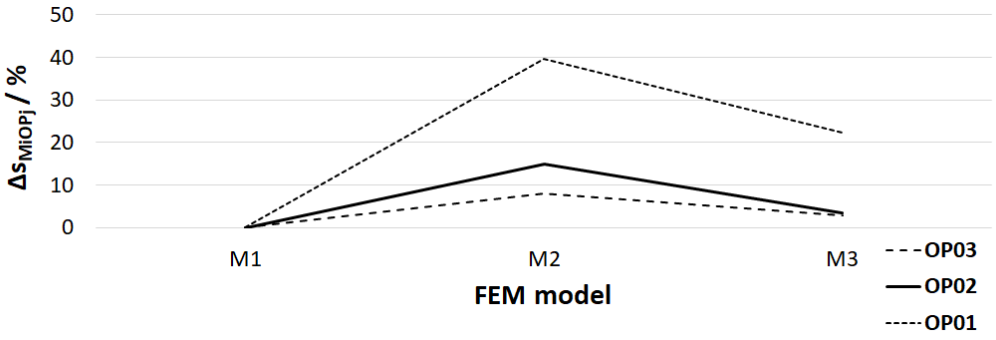

Figure 9 Influence of the different calculation models on the value of tip clearance

clearances of the FE models of the assembly to the reference model results from the quotient of the calculated tip clearance of the model M_i at operating point OP_j and the calculated tip clearance of the reference model M_1 at the same operating point OP_j, using:

$$\Delta s_{M_i OP_j} = \left(\frac{s_{calc_{M_i OP_j}}}{s_{calc_{M_1 OP_j}}} \right) \cdot 100 - 100 \tag{10}$$

The effect described can be seen most clearly in OP01, shown in Figure 9. Looking at the deviation at OP01 between the single impeller model (M_1) and the calculation model of the rotating system, the deviation of the tip clearance with the shaft assumed to be cold (M_2) is just under 40%, with the shaft assumed to be hot (M_3) the value is almost halved to 22%.

Shares of the individual loads in the axial deformation

For a good prediction of the resulting tip clearance during operation, it is essential to estimate the influence of the individual acting loads on the value of the maximum axial deformation. In the investigated case, an initial displacement of around six hundredths of a millimeter in the negative direction is shown due to the effect of a compression of the hub as a result of the preload, which results from the tightening torque when the impeller is mounted on the shaft. As this effect occurs in a stationary state, it is a constant value independent of the operating point and corresponds to a zero-point shift, which is shown in Figure 10.

While Figure 10 in a) shows the absolute proportions at the operating points analyzed, it shows in b) the relative proportion of the load in the axial deformation achieved at the respective operating point. The respective share βi in the maximum axial deformation is calculated from the difference between the maximum axial deformation of the i-th load component δx_{max_i} and the same without this load component $\delta x_{max_{(i-1)}}$, divided by the sum of all load shares in the maximum axial deformation δx_{max}, using:

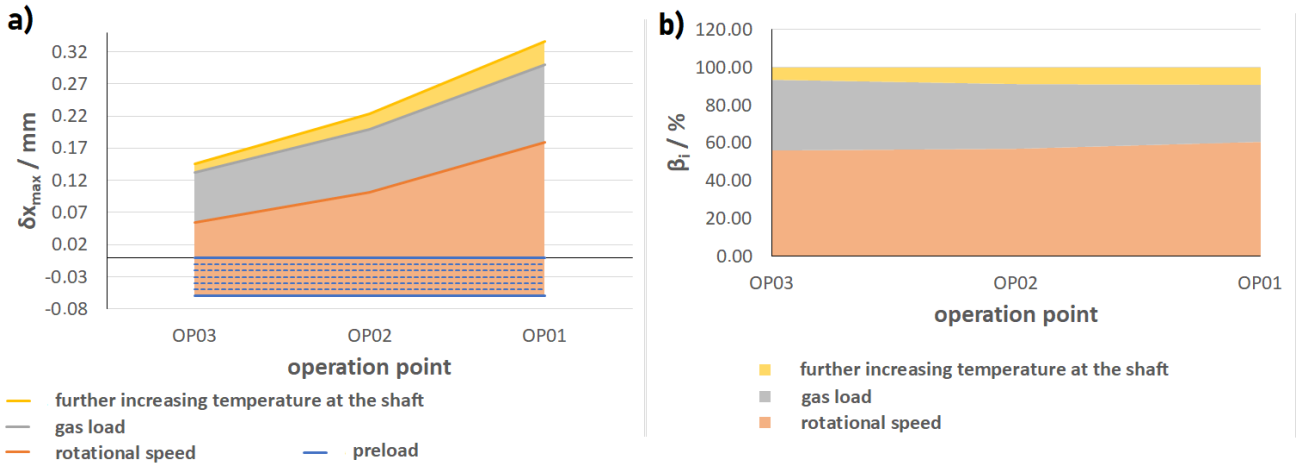

Figure 10 Maximum absolute values of the proportional axial displacement at the trailing edge (a) and Relative shares of the loads in the maximum axial deformation (b) at different operating points at different operating points

$$\beta i = \left(\frac{\delta x_{max_i} - \delta x_{max_{(i-1)}}}{\delta x_{max}} \right) \cdot 100 \tag{11}$$

It can be seen that the proportions at the various operating points differ only slightly from one another. The centrifugal force due to the rotational speed accounts for the largest proportion of the axial displacement at more than 55%. This proportion increases slightly with increasing speed up to 60%. The second largest proportion is the sum of the acting gas loads at more than 30%, whereby the temperature outside the impeller is close to the gas temperature at the compressor inlet. As the speed increases, this proportion decreases slightly from 38% to 31%. An additional temperature load outside the impeller towards the gas temperature at the impeller outlet results in the last component of the axial deformation, which is also the smallest component at less than 10%. This proportion tends to increase with increasing speed from 6% to 9%. The displacement components due to the temperature loads are always directly dependent on the distance between the impeller and the fixed bearing point. These values show that, contrary to common assumptions from studies on impellers with large diameters and blade heights, the exclusive use of the rotational speed is not sufficient for the H2C analysis in the specific case of a water vapor compressor in a high-temperature heat pump. Veining in the proportions is therefore to be expected with other designs.

Tip clearance in partial load operation and effect on the performance values

The initial hypothesis of these investigations was an expected large influence of the tip clearance on the aero performance values of the compressor due to the small blade heights at the impeller outlet. In order to answer this question, the performance values were calculated for the real expected axial clearances. For the sake of simplicity, it is assumed that the maximum value of the axial deformation represents a constant gap between the impeller and housing. In the optimization process chain for the design, an optimum tip clearance of 0.3 mm was assumed at all operating points, which results in a pressure ratio π_{tt} of 2,801, defined as the quotient of the total pressure at the impeller outlet p_{2t} and the total pressure at the compressor inlet p_{1t} , using:

$$\pi_{tt} = \frac{p_{2t}}{p_{1t}} \tag{12}$$

and an efficiency $\eta_{is,noleak}$ of 78,784%, defined as the quotient of isentropic total enthalpy change at the outlet $\Delta H_{t,is}$ to total enthalpy change at the compressor inlet ΔH_t, using:

$$\eta_{is} = \frac{\Delta H_{t,is}}{\Delta H_t} \tag{13}$$

at operating point OP01 and forms the reference. The values are added in Figure 11 for lines OP01, marked with RP_{opt}. Figure 11 shows the aero-performance at different tip clearances plotted at the considered operating points. The absolute values Figure 11(a) show hardly any change with changing tip clearance, as can also be seen in Table 4. To illustrate this, the change is plotted again as a relative value in Figure 11(b), whereby the values of the single impeller model form the reference, as the tip clearance in this model is the smallest and therefore the maximum is present in the aero performance values. The drop in the values due to the change in tip clearance as a result of the real axial deformation of the rotating assembly of the compressor is below the value of 1.5% in all analyzed points. The largest calculated loss occurs in the pressure ratio in OP01 at 1.4%.

CONCLUSIONS AND OUTLOOK

In this study, the influence of various components of the rotating assembly of a turbo radial compressor on tip clearance was analyzed and partial load operation was also considered. Based on the theoretical principles of the morphing method, the geometry of the full model to be investigated was generated from the mesh data of the optimization process chain and the full model was remeshed. To estimate the resulting deviation in the axial deformation between the design model (H2C analysis) and the model of the geometry to be manufactured, which includes a new mesh and a further load in addition to geometry changes, a forward calculation (C2H analysis) was carried out without further components of the rotating system, thus creating the reference for comparison. Subsequently, a model was built from the assembly design and the axial deformation was calculated at three operating points. A detailed look at the shares of the loads in the maximum axial deformation shows that the rotational speed accounts for the largest share with more than 50%, followed by the gas loads with more than 30%. The remaining share is due to further thermal expansion with temperature increase outside the actual flow geometry and corresponds more to an axial displacement of the impeller. With the results of the maximum axial deformation, the new tip clearances at the operating points were calculated and transferred to the CFD simulation. With these values, the characteristic values of the total-total pressure ratio and the isentropic efficiency were recalculated and compared with the reference model. The assumption that the change in tip clearance due to the small blade heights has a major influence on the aero performance of the impeller could not be confirmed. A slight deterioration in the aero

Table 4 Influence of tip clearance on the aero performance values

		unit	OP03	OP02	OP01
single impeller model (M1)	tip clearance s_{calc}	mm	0.374	0.296	0.174
	pressure ratio π_{tt}	-	1.726	2.010	2.874
	efficiency η_{is}	%	81.464	81.293	79.289
Model of rotational system with minimum temperature (M2)	tip clearance s_{calc}	mm	0.404	0.340	0.243
	pressure ratio π_{tt}	-	1.716	1.991	2.835
	efficiency η_{is}	%	80.922	80.704	79.103
Model of rotational system with maximum temperature (M3)	tip clearance s_{calc}	mm	0.385	0.306	0.213
	pressure ratio π_{tt}	-	1.722	2.005	2.852
	efficiency η_{is}	%	81.217	81.163	79.224

performance can be recognized. However, in the analyzed design, this is a maximum of 1.4% decrease in the pressure ratio in OP01. The tip clearance of 0.3 mm originally assumed in the optimization process chain is never achieved in OP01.
The results still show uncertainties, which are to be eliminated in future investigations. For this purpose, it is necessary to extend the simulation model to a thermo-mechanical coupling calculation and to acquire knowledge about the temperature conditions in the area of the shaft, rear wheel space and bearings. Another factor influencing tip clearance that should be considered in the future is the thermal expansion of the stationary part of the compressor.
Three key findings can be derived from the investigations. Firstly, it has become clear that the pressure in the rear impeller chamber has a major influence on the result of the maximum axial deformation and has to be considered in the CSM part of the optimisation process chain.
Secondly, it has become clear that the small changes in tip clearance due to the influence of the neighbouring parts of the assembly have a much smaller influence on the aero performance parameters π_{tt} and η_{is} than expected, whereas different operating points show a large difference in the values. Active gap control depending on the operating point is an interesting

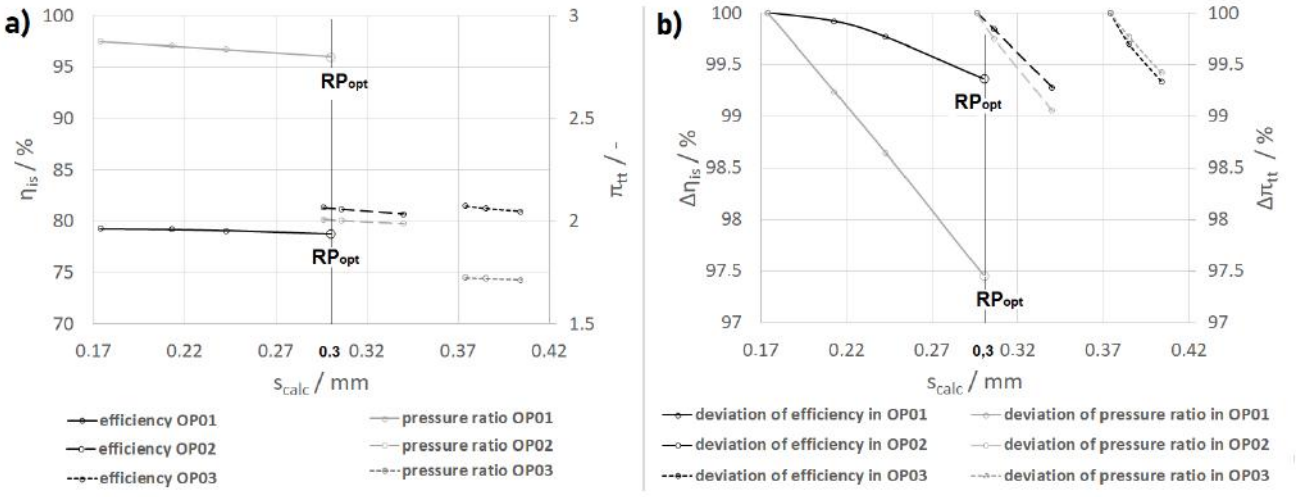

Figure 11 Influence of tip clearance on the aero performance values π_{tt} and η_{is} absolute (a) and standardised (b)

way of optimizing efficiency in part-load operation.
The third finding relates to the interplay between the thermal expansion of the shaft and its preload. Both effects cause a displacement of the impeller axially to the housing, but in opposite directions. Above a certain limit temperature, the thermal expansion will exceed the compression effect of the preload and reduce the tip cleanrance.

NOMENCLATURE

Acronyms and Abbrevation

calc	calculated value	–
CSM	Computational Structural Mechanics	–
FE	finite elemente	–
FEA	finite elemente analysis	–
HTHP	High Temperature Heat Pumps	
max	maximum	–
MPC	Multi Point Constraint	–
OP	operation point	–
opt	optimization	–
PC	definition of geometry by a set of points	–
red	reduced	–
rel	relative	–
rot	rotational	–
RP	reference point	–

Greek Letters

β	share of the load in maximum axial deformation	–
δ	nodal displacement	mm
$\Delta\delta x$	Absolute deviation of the maximum axial deformation	mm
ΔHx	change of enthalpie	J
Δs	deviation of tip clearance	–
δx	axial deformation	mm
ε	deviation	–
η	efficiency	–
μ	friction oefficient	–
Π	pressure ratio	–
ϑ	temperature	C

Roman Letters

E	mesh error according to RICHARDSON	–
p	pressure	Bar(a)
B	convergence order	–
D	diameter	mm
F	force	N
f	evaluation parameter for the mesh	–
H	enthalie	J
h	spatial discretization	–
i	counter, defined by $i = 1...n$	–
j	counter, defined by $i = 1...n$	–
M	torque	Nm
n	number	–
P	Thread pitch	mm
R	radius	mm
r	refinement ratio	–
s	tip clearance	mm

Superscripts n Subscripts

$1t$	total at compressor inlet	–
$2s$	static at compressor outlet	–
$2t$	total at compressor outlet	–
A	tightning	–
c	cold geometry	–
G	thread	–
H	hot geometry	–

h	high	–
is	isentrop	–
K	screw head	–
l	low	–
M	applies to model	–
M	mounted	–
m	middle	–
OP	applies to operation point	–
t	total	–
ts	total to static	–

REFERENCES

ANSYS, I. (2023), 'Ansys academic research mechanical release 23.1'.
URL: *https://www.ansys.com/de-de/academic/terms-and-conditions*

Casey, M. and Robinson, C. (2021), *Radial Flow Turbocompressors - Design, Analysis and Applications*.

Danish, S. N., Chaochen, M. and Yang, C. (2006), 'The influence of tip clearance on centrifugal compressor stage of a turbocharger'.
URL: *https://api.semanticscholar.org/CorpusID:195835949*

Decker, K.-H., Kabus, K., Rieg, F. et al. (2011), *Decker Maschinenelemente*.

Dhondt, G. (2022), 'Calculix - a free software three-dimensional structural finite element program'.
URL: *http://www.calculix.de/*

Gaun, L., Huppertz, A. and D., B. (2014), 'Hot-to-cold cad geometry transformation of aero engine parts based on b-spline morphing', *Turbo Expo: Power for Land, Sea, and Air* **2B**(1), V02BT45A020.
URL: *https://doi.org/10.1115/GT2014-26683*

Hazby, H., Woods, I., Casey, M. et al. (2015), 'Effects of blade deformation on the performance of a high flow coefficient mixed flow impeller', *Journal of Turbomachinery* **137**(12), 121005.
URL: *https://doi.org/10.1115/1.4031356*

Kamal, J. B. (2023), Investigation into the prediction of the service life of the impeller of a turbo radial compressor in a high temperature heat pump, Master's thesis, Brandenburgische Technische Universität (BTU) Cottbus-Senftenberg.

Maaß, C., Sandrock, D. M. and Fuß, G. (2018), Kurzgutachten: Strategische optionen zur dekarbonisierung und effizienteren nutzung der prozesswärme und -kälte, Technical report, Hamburg Institute.

myclimate foundation and Dellantonio, K. (2022), 'Wie gross ist der co_2-ausstoss der schweiz'. [Online; accessed 28th November 2023].
URL: *https://www.myclimate.org/de-ch/informieren/faq/faq-detail/wer-produziert-co2/*

Roache, P. J. (1994), 'Perspective: A method for uniform reporting of grid refinement studies', *Journal of Fluids Engineering* **116**(31), 405–413.
URL: *https://doi.org/10.1115/1.2910291*

Schaffrath, R., Kriese, M., Kajasa, B. et al. (2022), 'Multi operating point aerodynamic optimization of a radial compressor impeller for an application in high temperature heat pump', *Proceedings of ASME Turbo Expo 2022* **1 and ff**(1), 10.
URL: *https://elib.dlr.de/187572/1/v10dt34a011-gt2022-82130.pdf*

Schaffrath, R., Nicke, E., Forsthofer, N. et al. (2023), 'Gradient-free aerodynamic optimization with structural constraints and surge line control for radial compressor stage', *Proceedings of the ASME 2023* **1**(1), 2 and 6–7.
URL: *https://elib.dlr.de/196242/1/GT2023-101593.pdf*

Schwarzburger, H. and Alfons.W.GentnerVerlag (2022), 'Dlr nimmt hochtemperatur-wärmepumpe für industrieprozesse in betrieb'. [Online; accessed 02th September 2022].
URL: *https://www.photovoltaik.eu/waerme/dlr-nimmt-hochtemperatur-waermepumpe-fuer-industrieprozesse-betrieb*

Slater, J. W. (2021), 'SciPy: Examining spatial (grid) convergence'. [Online; accessed 02th November 2023].
URL: *https://www.grc.nasa.gov/WWW/wind/valid/tutorial/spatconv.html*

Umweltbundesamt (2024), ‘Treibhausgas-emissionen seit 1990 nach gasen’. [Online; accessed 28th November 2023].
URL: *https://www.umweltbundesamt.de/daten/klima/treibhausgas-emissionen-in-deutschland-emissionsentwicklung*

Wang, H.-l. and Xi, G. (2009), ‘Effect of Thermal and Mechanical Loads on the Centrifugal Impeller Deformation and Its Structure Optimization’, **Volume 5: Microturbines and Small Turbomachinery; Oil and Gas Applications**, 75–84.
URL: *https://doi.org/10.1115/GT2009-59280*

Zhihua, L., Zuo, Z., Li, W. et al. (2022), ‘Experimental and numerical analysis of the impeller backside cavity in a centrifugal compressor for caes’, *Journal of Fluids Engineering* **1**(1), 11.
URL: *https://www.mdpi.com/1996-1073/15/2/420*

és Gazdaságtudományi Egyetem, B. M. (2018), ‘Index of gyebro files ans help v182 ans thry’. [Online; accessed 12th Januar 2023].
URL: *https://www.mm.bme.hu/-gyebro/files/ans-help-v182/ans-thry/*

APPENDIX A - Overview of the material characteristics for FE model

Table 5 values of material properties used in model (Kamal, 2023)

	unit	Ti-6l-4V	18CrNiMo7-6	2007 Aluminum	100Cr6	9SMnPb28K	X10CrNi18-8
Density	$\frac{kg}{m^3}$	4430	7850	2770	7400	7900	7850
coefficent of thermal expansion	k^{-1}	9.4e-6	1.2e-5	2.3e-5	1.2e-5	1.2e-5	1.2e-5
Modulus of elasticity	Pa	1.138e11	2.1e11	7.1e10	2.0e11	2.1e11	1.865e11
Bulk modulus	Pa	1.2e11	1.75e11	6.96e10	1.67e11	1.75e11	1.55e11
Sheer modulus	Pa	4.24e10	8.08e10	2.67e10	7.69e10	8.08e10	7.17e10
Fatigue strength coefficient	Pa	1.64e9	9.2e8	-	9.2e8	9.2e8	9.2e8
Fatigue strength exponent	-	-0.09	-0.106	-	-0.106	-0.106	-0.106
Fatigue ductility coefficient	-	0.249	0.213	-	0.213	0.213	0.213
Fatigue ductility exponent	-	-0.56	-0.47	-	-0.47	-0.47	-0.47
Cyclic strength coefficient	Pa	9.85e8	1.00e9	-	1.00e9	1.00e9	1.00e9
Strain hardening exponent	-	0.0345	0.2000	-	0.2000	0.2000	0.2000
Tensile yield strength	Pa	8.80e8	3.35e8	2.40e8	5.00e8	3.70e8	1.20e9
Compressive yield strength	Pa	9.7e8	3.5e8	3.0e8	6.0e8	4.5e8	1.8e9
Ultimate tensile strength	Pa	9.5e8	1.2e9	3.5e8	9.0e8	4.4e8	1.6e9
Elongation at break	%	14.0	-	-	-	-	-
Poisson's ratio	-	0.342	0.290	0.330	0.300	0.300	0.300

APPENDIX B - Overview of Contact definition within FE-Model

Table 6 contact definition within FE-model

Contact	Target	contact type	friction coefficient
spinner	shaft	bonded	-
shaft	inner shell of ball bearings	bonded	-
shaft	impeller	frictionless	-
shaft	support ring	frictionless	-
inner clamping ring	spinner	frictional	0.3
shaft	inner clamping ring	frictional	0.3
inner clamping rinf	outer clamping ring	frictional	0.3
impeller	outer clamping ring	frictional	0.3
impeller	support ring	frictional	0.3
inner shell of ball bearing	support ring	frictional	0.3
support ring	inner shell of ball bearing	frictional	0.3

APPENDIX C - COPYRIGHT/OPEN ACCESS

APPENDIX D - GPPS Presenter Policy and Paper Acceptance

According to GPPS's presenter attendance policy, a paper cannot be published or be indexed and may not be cited as a published paper until at least one author pays the registration fee and attends the conference. The GPPS reserves the right to withdraw from its publications any paper not presented by an author of the paper at the appropriate conference. Any paper that is withdrawn may not be cited as a published paper.